Fuel mobility dynamics and their influence on applied smouldering systems

Seyed Ziaedin Miry [a,b,*], Marco A.B. Zanoni [a], Tarek L. Rashwan [c,d], Laura Kinsman [e], José L. Torero [d], Jason I. Gerhard [a,1]

[a] Department of Civil and Environmental Engineering, The University of Western Ontario, London, Ontario N6A 5B9, Canada
[b] Western Academy for Advanced Research, Western University, International and Graduate Affairs Building, Suite 3N54, London, Ontario N6A 3K7, Canada
[c] School of Engineering and Innovation, The Open University, Milton Keynes, MK7 6AA, UK
[d] Department of Civil, Environmental and Geomatic Engineering, University College London, London WC1E6BT, UK
[e] Savron, Toronto, Ontario M8 × 1Y9, Canada

ABSTRACT

Many recent environmentally beneficial applications of smouldering treat hazardous organic liquid fuels in inert porous media. In these applications, organic liquid mobilization can affect the treatment process, and the dynamics are poorly understood. Organic liquid mobilization is therefore a key knowledge gap that hinders the optimization of applied smouldering. This is especially the case in large scales where mobilization appears to be more significant. Liquid mobilization inside a porous medium cannot be easily measured directly, therefore numerical modelling is essential to understand the fundamental processes and to clarify the effects and dynamics of the fuel mobilization on the smouldering reaction. Contrasting numerical models with experimental temperature measurements has revealed many aspects of smouldering that cannot be measured. In this study, a previously developed 1D smouldering model was equipped with multiphase flow equations and compared against laboratory column experiments. The combination of model and experiments has served to quantify the dynamics of organic liquid fuel mobility by simulating high (i.e., non-mobile) and low (i.e., mobile) viscous fuels. The findings from this study shed light on the complicated interplay between multiphase flow, heat and mass transfer, and smoulder chemistry common to many applied smouldering systems. Numerical results confirmed that increasing the viscosity results in fuel remaining in the reaction zone and led to an increase in the peak temperature and smouldering front velocities. Lower viscosity fuels mobilized away from the reaction zone, thereby accumulating fuel in the pre-heating zone of the reactor. The fundamental understanding generated from this research will improve the design, implementation, and optimization of smouldering-based technologies for environmentally beneficial applications worldwide.

1. Introduction

Organic liquid wastes from industrial activities (e.g., oil sludge, coal tar, and oil-based drilled cuttings) are produced in large quantities (60 million tons per year) and >1 billion tons of this hazardous waste has been stockpiled worldwide [1]. This accumulated waste poses a looming threat to ecosystems and communities through environmental contamination [2]. Common organic liquid waste treatment methods are (*i*) incineration [3], (*ii*) pyrolysis [4], and (*iii*) gasification [5], which all typically require continuous supplies of additional energy, or waste pre-conditioning.

Applied smouldering combustion was introduced for a variety of applications, including (*i*) energy and resource recovery [6,7], (*ii*) waste-to-energy [8], (*iii*) pyrolysis and gasification (e.g., for CO and H_2 production) [9-11], also a (*iv*) new treatment approach for these organic liquid wastes, where the waste is mixed with an inert porous medium (e. g., sand) to form a smoulderable mixture for treatment [1,2,12]. Smouldering combustion is a highly efficient and flameless form of combustion driven by exothermic oxidation reactions at the surface of condensed fuels [13]. In smouldering applications, heat and air are initially supplied to a localized ignition region until the onset of a smouldering reaction. Once smouldering is ignited, the external heat supply is removed, and the smouldering front propagates in a

---

Nomenclature

Latin Letters

A	Pre-exponential factor, s^{-1}
A_s	Surface area, m^2
C_p	Specific heat capacity, J kg^{-1} K^{-1}
d_p	Particle diameter, m
D_g	Diffusion coefficient, m^2 s^{-1}
E	Activation energy, kJ mol^{-1}
G	Gravity, m s^{-2}
h_{sg}	Interfacial heat transfer coefficient, W m^{-2} K^{-1}
K	Thermal conductivity, W m^{-1} K^{-1}
k_i	Intrinsic permeability, m^2
k_r	Relative permeability, m^2
L	Fuel bed length, m
M_g	Molar weight, g mol^{-1}
M	Total Mass, kg
Nu	Nusselt number
P	Pressure, Pa
P_d	Displacement pressure, Pa
Pr	Prandtl number
Q	Darcy Flux, m s^{-1}
$\dot{q}$	Heat flux, W m^{-2}
R	Reaction rate, s^{-1}
Re	Reynolds number
R_g	Ideal gas constant, J mol^{-1} K^{-1}
S	Saturation
S_e	Effective saturation
T	Temperature, °C
U	Radial heat transfer coefficient, W m^{-2} K^{-1}
ν_c	Char mass yield, kg.Char kg.Canola oil^{-1}
ν_f	Smouldering front velocity, cm min^{-1}

ν_{O_2}	Oxygen mass yield, kg.O$_2$ kg.Char^{-1}
Y	Mass fraction

Greek Symbols

ΔH	Heat of reaction, MJ kg^{-1}
μ	Dynamic viscosity, Pa s
ρ	Density, kg m^{-3}
ϕ	Porosity
σ	Stefan-Boltzmann constant, W m^{-2} K^{-4}
τ	Time scale
λ	Pore size distribution

Subscripts/Superscripts

AVG	Average
B	Bulk
C	Char
Cl	Cylinder
Cri	Critical
Eff	Effective
F	Flow
G	Gas
In	Inlet
N	Non-wetting phase (i.e., Air)
P	Pyrolysis
Peak	Peak
Rad	Radiation
S	Solid
Sp	Spherical
Rad	Radiation
W	Wetting phase (i.e., Canola Oil, Canola Oil with VI improver, VI Improver)
0	Initial value

"self-sustaining" manner without further external energy as long as the local rate of energy released overcomes local heat loss rates [14].

Fuel mobility plays an important role in applied smouldering systems. Mobility affects key characteristics (e.g., temperature and fuel saturation distribution, and smouldering front velocity), which might be desirable (e.g., to deposit more fuel in the reaction zone for accelerated treatment) or undesirable (e.g., upward mobility can increase fuel saturation in the preheating zone, decrease the air permeability, and lead to processing challenges). For example, an experimental smouldering study treating organic liquids identified undesirable fuel mobility effects where mobility led to erratic temperatures and poor process controllability [15]. In this case, downward mobility of low viscous fuel from an extended preheating zone (> 10.5 cm) to the reaction zone (*i*) caused rapid cooling and reignition; (*ii*) stalled the trailing edge of the smouldering front, which effectively thickened the smouldering reaction zone; and (*iii*) led to rapid increases in peak temperatures (i.e., due to super-adiabatic effects) [15]. These effects from mobility still need to be further investigated, as the governing mechanisms are not well-understood.

In a similar but separate context, fuel mobility occurs in enhanced oil recovery systems to extract high viscous, heavy oil and bitumen from natural geological formations [16]. The energy generated from smouldering is transferred ahead to preheat oil and decrease its viscosity and promote mobilization toward extraction wells [17,18]. In these studies, fuel mobility in the preheating zone caused separate challenges. For example, fuel accumulation from uncontrolled mobility clogged pores, which decreased the air permeability and restricted air flow below a critical point where oxidation reactions could not be self-sustained [1, 19-22].

Fig. 1 illustrates the fuel mobility dynamics for a typical upward-forward smouldering propagation system. Four main zones can be identified: (*i*) virgin fuel zone, (*ii*) preheating zone, (*iii*) reaction zone, and (*iv*) cooling zone. In the virgin fuel zone, high viscosity fuels are immobile at ambient temperatures, while low viscosity fuels at ambient temperature can either be immobile or mobilize downwards due to gravity effects. In the preheating zone, downward mobility can occur due to gravity and decreased viscosities with elevated temperatures. Moreover, upward mobility can take place due to upward forces caused by the applied air flow. In the reaction zone, fuel is pyrolyzed and oxidized to produce heat and gases. In the cooling zone, typically only hot clean sand remains with no residual fuel [23].

As many applied smouldering applications treat hazardous organic liquids, fuel mobility effects are routinely observed; however, the governing physics are poorly understood. For example, the interplay between fuel, air, and porous media on mobility and smouldering behaviour has not been well-explained. Lessons from other applications, e.g., enhanced oil recovery, can assist in understanding this phenomenon, but ultimately more research is needed to understand fuel mobility effects in applied smouldering systems. This is a key knowledge gap and the main motivation for this research.

Many numerical modelling studies have recently improved the understanding of conditions that govern the success of applied smouldering systems [11,14,24,25]. One-dimensional (1D) smouldering models have been extensively used to explore the effect of chemical dynamics [26-28]. These models provide valuable insights into the fundamental reaction kinetics and extinction criteria [14,29,30]. However, to better understand the complexities of smouldering combustion in practical scenarios, two-dimensional (2D) numerical models have been developed. These 2D models demonstrate the significant effects of radial heat losses on the multi-dimensional transfer effects of
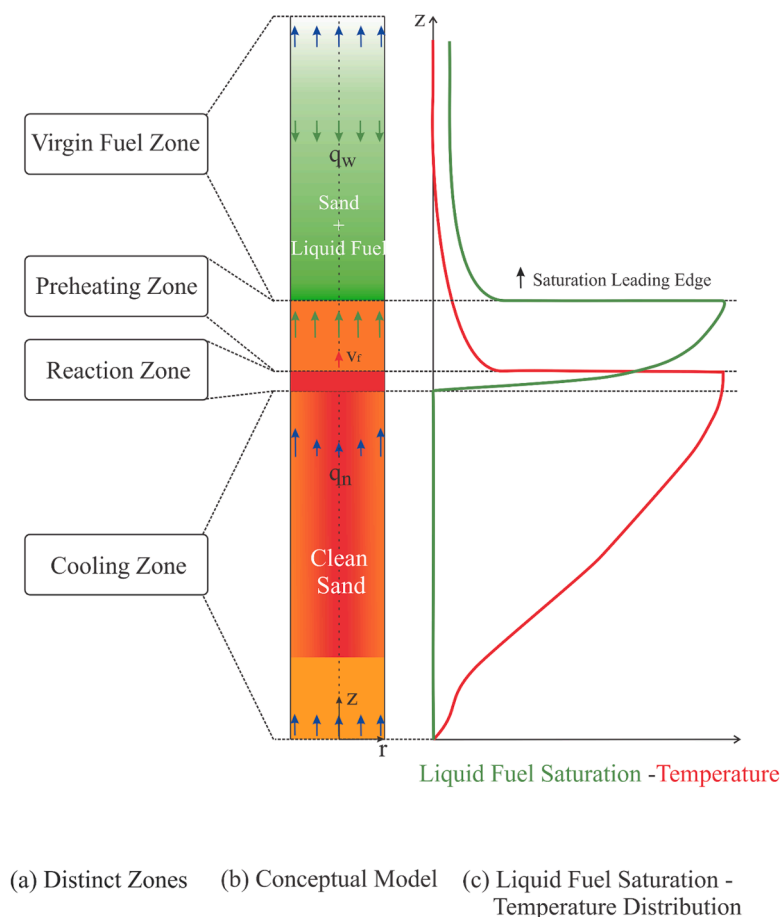
Fig. 1. Conceptual model of liquid fuel saturation distribution with forward-upward smouldering propagation. (a) The key distinct zones including virgin fuel, preheating, reaction, and cooling zones are determined, (b) the conceptual model where the blue, red, and green arrows represents air flow, smouldering front velocity, and liquid fuel flow, respectively, along with associated (c) liquid fuel saturation and temperature distribution.

temperature [31-34], air flux [35,36], oxygen mass fraction [37,38], heat release rate [34], and chemistry distribution that affect the smouldering front shape, velocity, propagation, peripheral extinction, and global quenching [31,32,36,39]. However, none of these 1D and 2D models investigated fuel mobility, even though it is a major concern during industrial treatment of hazardous organic liquids [12,15,40].

This study tackles this knowledge gap via equipping a previously developed 1D numerical model with key multiphase flow equations to model fuel mobility in an applied smouldering system [14]. Experimental results from canola oil smouldering (i.e., a low viscosity surrogate fuel) were used to calibrate the model. The calibrated model was then validated via experiments with a fuel mixture of canola oil and viscosity index (VI) improver (i.e., an additive to increase viscosity). As fuel concentrations are not routinely tracked over space and time, temperature histories were used for model calibration and validation. The effects of mobility were explored by simulating smouldering with high (i.e., non-mobile) and low (i.e., mobile) viscosity fuels. Sensitivity analyses were performed to better understand the effects of fuel (e.g., initial saturation, viscosity), air (e.g., Darcy air flux), and porous media (e.g., intrinsic permeability, pore size distribution index, and length of the fuel bed) on key aspects of applied smouldering systems that are both fundamental (e.g., peak temperature, front velocity, saturation leading edge, and oxygen consumption) and practical (e.g., robustness, and global extinction). Global and local energy analyses were performed to quantify all effects. Altogether, this study provides novel insights into the dynamics and effects of liquid fuel mobilization in applied smouldering systems, which supports the improved design, implementation, and optimization of smouldering-based technologies.

2. Methodology

2.1. Experiments

Three smouldering experiments were conducted by Kinsman et al. [15] in a laboratory-sized reactor using organic liquid fuels with different viscosities to evaluate the effects of fuel mobility on smouldering. First, pure canola oil (non-toxic low viscosity fuel, 0.07 Pa s, Exp. # *i*, Table 1) was used to demonstrate a smouldering system that was highly affected by fuel mobility. Then, a 1:1 mixture (i.e., with a mass ratio of 0.5 kg kg^{-1}) of canola oil to viscosity index (VI) improver (V-158, Tempo Canada ULC) was used to increase the mixture viscosity to 1.32 Pa s (Exp. # *ii, iii*, Table 1). VI improver was used to reduce downward mobility to approximately represent the mobility expected in smouldering systems with oil sludge and coal tar [15].

The stainless-steel reactor was 16 cm in diameter and 64 cm tall, where 30 cm tall fuel beds were used. Quartz sand (#12ST, Bell and Mackenzie Co. Ltd., Canada) with a bulk dry density of 1600 kg m^{-3} and mean grain size of 0.88 mm was used in all experiments. A mass ratio of 0.06 kg kg^{-1} of organic liquid mass to sand mass was used in all experiments, with a saturation (S_w) of 0.30, based on the average measured sand porosity ($\phi = 0.38$). Note that there were minor differences between the saturations with and without VI added due to the small impact of the fuel density variations. The initial saturation for canola oil: VI improver was $S_w = 0.27$ to account for VI improver density.

The effects of water evaporation and condensation on smouldering systems were not considered in this study due to negligible initial moisture content of the fuel [41]. The thermocouples (Type K, Inconel,

Table 1
List of the experiments and simulations performed in the sensitivity analysis.

Exp. # (repeats)	Simulation #	Fuel Type	Darcy Air Flux ($q_{n,in}$, m s^{-1})	Initial Saturation (S_w)	Intrinsic Permeability (k_i 10^{-10}, m^2)	Viscosity (μ, Pa s)	Pore Size Distribution Index (λ)	Fuel bed Length (L, m)
i (3)	1 (Base Simulation)	Canola oil	0.058	0.30	5.0	0.07	2.5	0.30
ii (3)	2	Canola oil with VI improver	0.062	0.27	5.0	1.32	2.5	0.30
iii (1)	3		0.025	0.27	5.0	1.32	2.5	0.30
–	4	VI improver	0.058	0.30	5.0	31.04	2.5	0.30
–	5	Canola oil	0.040	0.30	5.0	0.07	2.5	0.30
–	6		0.080	0.30	5.0	0.07	2.5	0.30
–	7		0.025	0.30	5.0	0.07	2.5	0.30
–	8		0.058	0.20	5.0	0.07	2.5	0.30
–	9		0.058	0.40	5.0	0.07	2.5	0.30
–	10		0.058	0.30	2.5	0.07	2.5	0.30
–	11		0.058	0.30	10	0.07	2.5	0.30
–	12		0.058	0.30	5.0	1.32	2.5	0.30
–	13		0.058	0.30	5.0	0.07	1	0.30
–	14		0.058	0.30	5.0	0.07	4	0.30
–	15		0.058	0.30	5.0	0.07	2.5	0.15
–	16		0.058	0.30	5.0	0.07	2.5	0.90

Omega) were placed at the centerline spaced 3.5 cm apart, where the first thermocouple (TC1) was located 1.0 cm above the heater and 11 cm above the gas diffuser (see Fig. 2a). Temperatures were recorded at two seconds intervals using a data logger (Multifunction Switch/Measure Unit 34980A, Agilent Technologies). Schematics of the experimental setup and computational domain are shown in Fig. 2, which were detailed previously [15].

A standard ignition procedure was used in each experiment [42]. That is, a localized area was heated with an Inconel-sheathed electrical cable heater (Waltow, USA, 450 W), which was coiled into a flat spiral and placed above the gas diffuser. The heater power was increased in 25 W increments every 10 min from an initial power of 290 W to 415 W, until the first thermocouple ($x = 0.11$ m) reached 360 °C (i.e., the approximate smouldering ignition temperature of canola oil [15]) after approximately 90 min. At this stage, air was injected at $t = t_g$ into the column using an air diffuser placed at the bottom of the column ($x = 0.00$ m) at a fixed rate. Then, smouldering ignition occurred, as seen by the rapidly increasing temperature of the first thermocouple (TC1). The heater was then turned off at $t = t_h$ after TC1 reached its peak temperature (570 °C), while the air remained on to support the self-sustaining smouldering propagation. The differences in ignition conditions (i.e., air/heater on/off times) only led to small differences in initial effects and did not influence the main trends studied. Table 1 shows the list of experiments and their corresponding simulations. Note that all experiments supported self-sustaining smouldering.

To compare between experimental results and numerical simulations, time (t) was normalized as a dimensionless time (Dt) [30] to account for differences in the average smouldering front velocities (ν_f) calculated using the procedure from [42] with fuel bed lengths (L) and ignition times (t_g) [15,30]. The length (z) was normalized to account for the difference in the fuel bed length (see Table 2).

The non-dimensional times and time frames: (*i*) Dt < 0, (*ii*) Dt = 0, (*iii*) 0 < Dt ≤ 1, and (*iv*) Dt > 1 represent the following: (*i*) preheating; (*ii*) smouldering ignition (i.e., start of air injection); (*iii*) smouldering propagation over the initial fuel bed length; and (*iv*) smouldering propagation above the initial fuel bed length, due to fuel mobility and deposition into initially clean sand. (*i*) – (*iii*) were explained in detail in [24] and (*iv*) is discussed in detail in Section 3.2. The parameters are explained in Table 3.

2.2. Modelling

A previously developed 1D numerical model in COMSOL Multiphysics (Version 6) [14] was equipped with multiphase flow equations to simulate the migration of an organic liquid fuel in a porous medium under smouldering conditions. This model used a resolution of 0.05 cm mesh size.

The computational domain simulated: (*i*) a porous medium of clean sand at the bottom and top of the reactor with 11 and 21 cm thicknesses, respectively, and (*ii*) a porous medium composed of clean sand mixed with canola oil (or canola oil with VI improver) with 30 cm thickness. The governing equations (Eqs. (3)-29) were solved at every node in space and time, where three main phases were considered: (*i*) solid (i.e., sand and char produced by canola oil pyrolysis), (*ii*) liquid (wetting phase: canola oil or canola oil with VI improver), and (*iii*) gas (non-wetting phase: air). Canola oil chemical kinetics followed a global, two-step reaction mechanism (see Supplementary Material, Section A) where canola oil was pyrolyzed to char and the char was oxidized.

$$Canola\ Oil \overset{R_p}{\rightarrow} \nu_c\ Char + (1 - \nu_c)\ Gas \tag{3}$$

$$Char + \nu_{O_2} O_2 \overset{R_c}{\rightarrow} Gas \tag{4}$$

Pyrolysis (R_p) and oxidation reaction rates (R_c) were described by first-order Arrhenius reactions [43]:
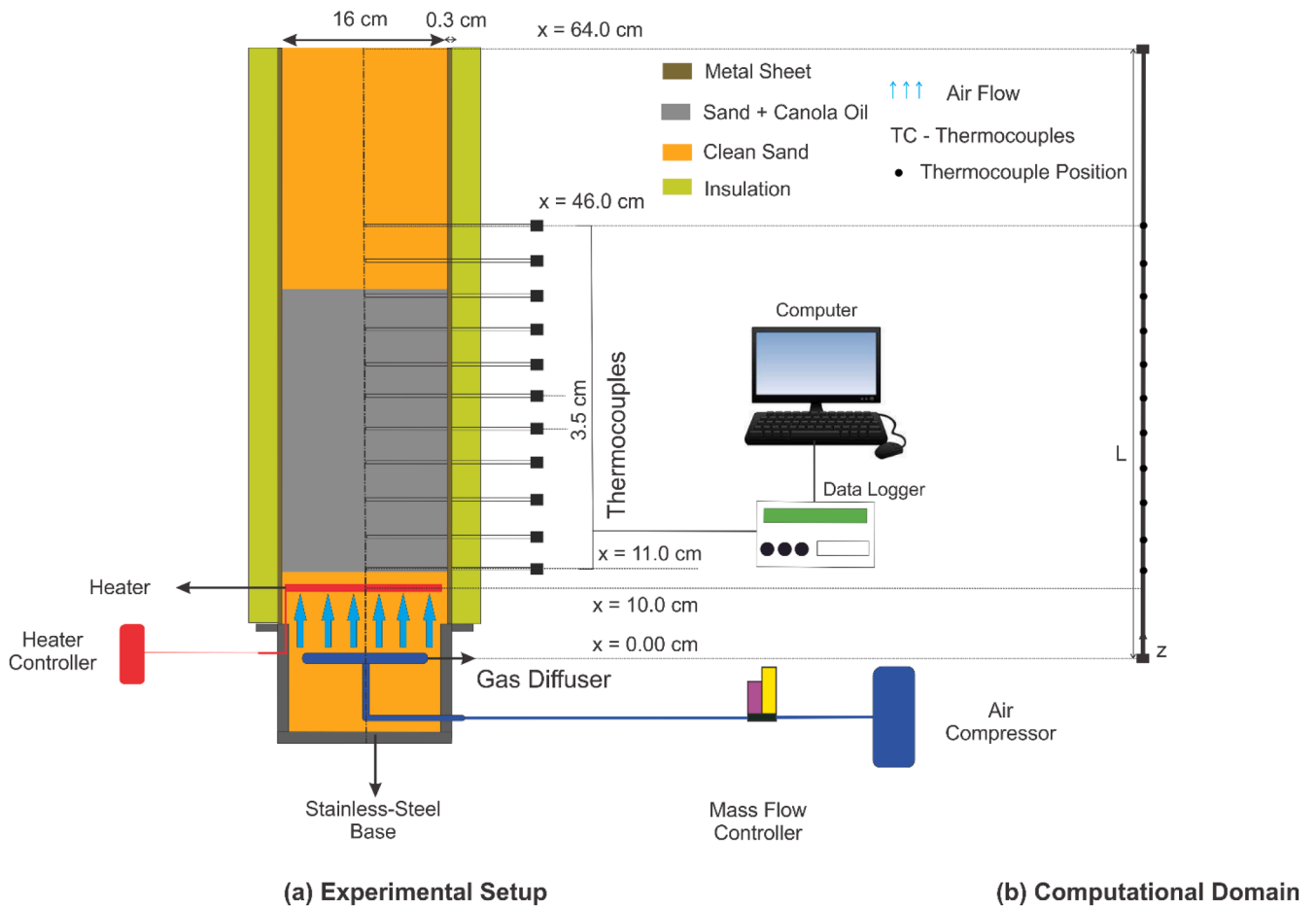
Fig. 2. Schematic view of (a) experimental setup and (b) computational domain.

Table 2
Dimensionless parameters used in smouldering experiments and simulations.

Parameter	Eq.	
Time	$Dt = \dfrac{(t - t_g)\nu_f}{L}$	(1)
Length	$Dz = \dfrac{z}{L}$	(2)

$$R_p = A_p exp\left(-\frac{E_p}{R_g T_w}\right)(Y_w) \tag{5}$$

$$R_c = A_C exp\left(-\frac{E_C}{R_g T_w}\right)(Y_{char})(Y_{O_2}) \tag{6}$$

where A_p and A_c are pre-exponential factors; E_p and E_c are the activation energies for pyrolysis and oxidation reactions, respectively; T_w is the wetting phase temperature (i.e., canola oil), which was assumed to be in local thermal equilibrium with sand temperature (i.e., see Eq. 23); and ν_c and ν_{O_2} are the char and oxygen mass yields, respectively. The canola oil and oxygen mass fractions were defined as $Y_w = m_{Canola\ oil}/m_{Canola\ oil,0}$ and $Y_{O_2} = m_{O_2}/m_{air}$, respectively. The subscripts s, w, and n note the solid (i.e., sand), wetting phase (i.e., canola oil), and non-wetting phase (i.e., air), respectively.

The pressure and saturation distributions were solved as functions of space and time, subject to inertial, gravity, and capillary forces considering the influences of soil intrinsic permeability, relative permeabilities, and temperature-dependent organic liquid viscosity. The conservation of mass for the wetting phase (i.e., canola oil), char, and non-wetting phase (i.e., air), was defined by Eqs. (7), 10, and 11 [44]:

$$\frac{\partial(\phi S_w \rho_w Y_w)}{\partial t} + \frac{\partial(\rho_w q_w)}{\partial z} = -Q_w \tag{7}$$

where ϕ, S_w, ρ_w, and q_w are porosity, canola oil saturation, canola oil density, and Darcy flux of canola oil, respectively. Q_w (i.e., volumetric mass consumption rate from canola oil pyrolysis), and Y_w were defined by [14]:

$$Q_w = \phi\ S_w\ \rho_w\ R_p \tag{8}$$

$$\frac{\partial(Y_w)}{\partial t} = -R_p \tag{9}$$

The char conservation of mass was [14]:

$$\frac{\partial(Y_c)}{\partial t} = \nu_c\ R_p - R_c \tag{10}$$

Porosity of canola oil is defined by [14]:

$$\phi_w = \phi S_w Y_w \tag{11}$$

where ϕ_w is dynamically updated when canola oil was pyrolyzed, i.e., as Y_w decreases from 1 to 0, which reflected the mass loss due to pyrolysis. The conservation of mass for non-wetting phase (i.e., air) was [44]:

$$\frac{\partial(\phi \rho_n S_n)}{\partial t} + \frac{\partial(\rho_n q_n)}{\partial z} = Q_n \tag{12}$$

Where S_n, ρ_n, and q_n are the saturation, density, and Darcy flux of air, respectively. Q_n represents the volumetric mass generation rate and was defined by [14]:

Table 3
Numerical model input parameters.

Parameters	Value	Unit	Ref
$log\,(A_c)$	6.7560	$log(s^{-1})$	This work, measured
$log\,(A_p)$	9.3593	$log(s^{-1})$	This work, measured
C_{p_n}	$-3 \times 10^{-5}\,T_n^2 + 0.2261\,T_n + 940.35$	J kg^{-1} K^{-1}	[53]
C_{p_s}	$1.75\,T_w + 340.32$	J kg^{-1} K^{-1}	[51]
C_{p_w}	$5.3054\,T_w + 287.56$	J kg^{-1} K^{-1}	[54], correlated
d_p	0.88	mm	[15]
D_g	4.35×10^{-5}	m^2 s^{-1}	[55]
E_c	1.1143×10^5	kJ mol^{-1}	This work, measured
E_p	1.5119×10^5	kJ mol^{-1}	This work, measured
k_i	5×10^{-10}	m^2	[15]
k_s	$6.38 \times 10^{-4}\,T_w + 0.0915$	W m^{-1} K^{-1}	[51]
k_n	$-10^{-8}\,T_n^2 + 8.0 \times 10^{-5}\,T_n + 0.0043$	W m^{-1} K^{-1}	[53]
k_w	$9.0 \times 10^{-5}\,T_w + 0.1394$	W m^{-1} K^{-1}	[54], correlated
m_s	9.730	kg	[15]
m_w	0.551	kg	[15]
M_g	28.97	g mole^{-1}	[56]
p_d	204.6	Pa	[15]
ϕ	0.38	–	[15]
$\dot{q}$	25,000	W m^{-2}	[50]
ρ_s	2650	kg m^{-3}	[51]
ρ_w	920	kg m^{-3}	[24]
R	8.0	cm	[15]
R_g	8.314	J mol^{-1} K^{-1}	[51]
S_r	1×10^{-6}	–	[15]
$S_{w,0}$	0.30	–	[15]
T_∞	295	K	This work, measured
U	8	W m^{-2} K^{-1}	[50]
Σ	5.67×10^{-8}	W/m^2 K^4	[51]
ΔH_c	16	MJ kg^{-1}	This work, calibrated
ΔH_p	-3	MJ kg^{-1}	This work, calibrated
ν_c	0.9	–	This work, calibrated
ν_{O_2}	2.5	–	This work, calibrated
μ_n	$-9 \times 10^{-12}\,T_n^2 + 4 \times 10^{-8}\,T_n + 6 \times 10^{-6}$	Pa s	[57]
μ_w (canola oil)	$for\ 20 < T_w < 70°C$ $3.23 \times 10^7 exp(-0.0699\,T_w) + 6.152\exp(-0.01833\,T_w)$ $for\ 70 < T_w < 627°C$ 0.009	Pa s	[15], correlated
μ_w (canola oil: VI improver)	$for\ 20 < T_w < 70°C$ $-0.0192\,T_w + 6.9528$ $for\ 70 < T_w < 627°C$ 0.018	Pa s	[15], correlated
λ	2.5	–	[44]

$$Q_n = \phi\,S_w\,\rho_w\big([1 - \nu_c]\,R_p + R_c\big) \tag{13}$$

R_p and R_c are the pyrolysis and oxidation reaction rates defined by Eqs. (5) and 6, respectively. Capillary pressure-saturation functions were defined by Eqs. (14)-15 [45,46]:

$$S_w = \left(\frac{p_c}{p_d}\right)^{-\lambda}(1 - S_r) + S_r \tag{14}$$

$$S_n = 1 - S_w \tag{15}$$

Where p_d, S_r, and λ represent the displacement pressure, residual saturation (the minimum saturation where the maximum capillary pressure was achieved ($p_{c_{max}}$)), and pore size distribution index, respectively, and p_c is capillary pressure defined by Eq. (16).

$$p_c = p_n - p_w \tag{16}$$

p_w, and p_n are wetting and non-wetting pressure. Darcy's Law was used to determine the wetting and non-wetting phase velocities:

$$q_w = -K_w\frac{dh_w}{dz} = -\frac{k_{rw}\,k_i}{\mu_w}\left(\frac{\partial p_w}{\partial z} + \rho_w\,g\right) \tag{17}$$

$$q_n = -K_n\frac{dh_n}{dz} = -\frac{k_{rn}\,k_i}{\mu_n}\left(\frac{\partial p_n}{\partial z} + \rho_n\,g\right) \tag{18}$$

where K, h, k_r, k_i, μ, ρ, p, and g represent hydraulic conductivity, fluid head, relative permeability, intrinsic permeability, viscosity, density, pressure, and gravity, respectively.

The key factors were (*i*) phase hydraulic gradients (dh/dz), (*ii*) temperature-dependent liquid viscosity, (*iii*) porous medium intrinsic permeability, and (*iv*) relative permeability. The relative permeability for wetting and non-wetting phases were defined using traditional Brooks-Corey equations by [44]:

$$k_{rw} = S_e^{\left(\frac{2+3\lambda}{\lambda}\right)} \tag{18a}$$

$$k_{rn} = (1 - S_e)^2\left(1 - S_e^{\left[\frac{2+\lambda}{\lambda}\right]}\right) \tag{19}$$

where λ is pore size distribution index and S_e is the effective saturation [44]:

$$S_e = \frac{S_w - S_r}{1 - S_r} \tag{20}$$

The gas density was calculated via the ideal gas law [47]:

$$\rho_n = \frac{p_n}{R\,T_n} \tag{21}$$

where R is the gas constant. The bulk transport of oxygen in the gas phase was described by Eq. (22) [48]:

$$\frac{\partial(\phi S_n \rho_n Y_{O_2})}{\partial t} + \frac{\partial(\rho_n q_n Y_{O_2})}{\partial z} = \frac{\partial}{\partial z}\left(\phi S_n \rho_n D_g \frac{\partial Y_{O_2}}{\partial z}\right) + Q_{O_2} \tag{22}$$

where D_g is the oxygen diffusion coefficient, Q_{O_2} represents the mass per unit volume per unit time of oxygen consumed via Eq. (23):

$$Q_{O_2} = -\phi S_w \rho_w \nu_{O_2} R_c \tag{23}$$

The conservation of energy considered local thermal equilibrium (LTE) between condensed phases (i.e., sand, canola oil, and char) and local thermal non-equilibrium (LTNE) between the condensed phases and air [48-50]:

$$\left(\rho C_p\right)_{eff} \frac{\partial T_w}{\partial t} + \rho_w C_{p_w}\left(q_w Y_w \frac{\partial T_w}{\partial z}\right) = \frac{\partial}{\partial z}\left(k_{eff}\frac{\partial T_w}{\partial z}\right) + h_{nw}\left(\frac{A_{s,sp}}{V_{sp}}\right)(T_n - T_w) - U\left(\frac{A_{s,cl}}{V_{cl}}\right)(T_w - T_\infty) + Q_{gen} \tag{24}$$

$$\phi S_n \rho_n C_{p_n}\frac{\partial T_n}{\partial t} + \rho_n C_{p_n}\left(q_n\frac{\partial T_n}{\partial z}\right) = \frac{\partial}{\partial z}\left(\phi S_n k_n \frac{\partial T_n}{\partial z}\right) + h_{nw}\left(\frac{A_{s,sp}}{V_{sp}}\right)(T_w - T_n) \tag{25}$$

where $A_{s,sp}$ and V_{sp} are the specific surface area and volume of the sand, respectively.

$$\frac{A_{s,sp}}{V_{sp}} = \frac{6(1-\phi)}{d_p} \tag{26}$$

where d_p is particle diameter. Q_{gen} represents the volumetric energy consumption rate of canola oil pyrolysis (ΔH_p) and production rate from char oxidation (ΔH_c) defined by Eq. (27):

$$Q_{gen} = \phi S_w \rho_w \left(\Delta H_p R_p + \Delta H_c R_c\right) \tag{27}$$

The interfacial heat transfer coefficient (h_{sg}) was described by Eq. (28) [51]:

$$Nu = \frac{h_{sg}\, d_p}{k_g} = 0.001 \left(Re^{1.97}Pr^{\frac{1}{3}}\right) \tag{28}$$

Eqs. (29, 30, 31) assumed effective thermal properties in the bulk combinations of sand and canola oil [48]:

$$\left(\rho C_p\right)_{eff} = \phi_s \rho_s C_{P_s} + \phi\, S_w\, \rho_w C_{P_w} \tag{29}$$

$$k_{eff} = \phi_s(k_s + k_{rad}) + \phi\, S_w k_w \tag{30}$$

$$\phi_s = 1 - \phi \tag{31}$$

where ρ, ϕ, C_p, and k are the densities, porosities, heat capacities, and thermal conductivities, respectively. Char porosity was not considered in calculating ϕ_s, as its effect was assumed negligible because it was formed and simultaneously oxidized in the reaction zone eventually converted into gas. Radiative heat transfer was embedded in the effective solid conductivity following the Rosseland approximation ($k_{rad} = 16\sigma\, d_p T_s^3/3$) [51], where σ is the Stefan-Boltzmann constant [52]. The model parameters not described above are presented in Table 3, and the initial and boundary conditions are provided in Table 4. The heater was simulated by a constant heat flux delivered at the inlet boundary, as determined in the previous study [50]. The heat loss coefficient ($U = 8$ [W m^{-2} K^{-1}]) was based on a previous established methodology [24]. Global and local energy balances based on the approach developed by [14,30] were used and the equations are shown in Table 5.

In this work, correlations were defined for canola oil thermal conductivity (k_w), heat capacity (C_{p_w}), and viscosity (μ_w).

3. Results and discussion

3.1. Model calibration and validation

Fig. 3 shows a comparison of experimental results and numerical model predictions for different fuels (i.e., canola oil and canola oil with VI improver) and inlet Darcy air fluxes ($q_{n,in}$). Fig. 3a highlights the experimental results from canola oil smouldering with $q_{n,in} = 0.058$ m s^{-1} (i.e., Exp. # i, repeated 3 times). These experiments exhibited stable average peak temperatures ($T_{p,\, avg} = 557 \pm 4$ °C) and smouldering front

Table 4
Initial and boundary condition in the numerical model.

Eq.	Initial Condition ($t = 0$)	Boundary Condition
(7)	$\begin{cases} S_w = S_r \to 0.00 < z < 0.11 \\ \quad\quad\quad 0.41 < z < 0.63 \\ S_w = S_{w,0} \to 0.11 < z < 0.41 \end{cases}$	$z = 0.00 \to \begin{cases} \rho_w q_w = 0 \\ \rho_n q_n = \rho_n q_n(t) \begin{cases} q_n = 0 \to 0 \le t \le t_g \\ q_n = q_{n,in} \to t_g \le t \le t_f \end{cases} \\ -\left(k_{eff}\right)\frac{\partial T_w}{\partial z} = 0 \\ T_n = T_0 \\ Y_{O_2} = Y_{O_2,0} \end{cases}$
(9)	$Y_w = 1$	
(10)	$Y_c = 0$	
(11)	$P_n = 101,375\ Pa$	
(21)	$Y_{o2} = 0.23$	
		$z = 0.11 \to \begin{cases} -\left(k_{eff}\right)\frac{\partial T_w}{\partial z} = \dot{q} \to 0 \le t \le t_h \\ -\left(k_{eff}\right)\frac{\partial T_w}{\partial z} = 0 \to t_h \le t \le t_f \end{cases}$
(23)	$T_s = T_w = T_\infty$	
		$z = 0.64 \to \begin{cases} \frac{\partial P_w}{\partial z} = 0 \\ P_n = P_0 \\ -\left(k_{eff}\right)\frac{\partial T_w}{\partial z} = 0 \\ -\left(k_n\right)\frac{\partial T_n}{\partial z} = 0 \\ -D_g \frac{\partial(\rho_n Y_{O_2})}{\partial z} = \rho_n q_n\left(Y_{O_2,0} - Y_{O_2}\right) \end{cases}$
(24)	$T_g = T_\infty$	

Table 5
Local and global energy balance equations.

Energy Rate of	Eq. (Local)	Eq. (Global)	Eq.
Inlet ($\dot{E}_{in}$)	$\rho_n q_n \, C_{p_n}(T_{n_{(z1)}} - T_\infty)\pi \, R^2$ (for air)	$\dot{q}_{in(z=0.11)} \, \pi \, R^2$ (from heater)	(30)
	$\rho_w q_w \, C_{p_w}(T_{w_{(z2)}} - T_\infty)\pi \, R^2$ (for canola oil)		
Outlet ($\dot{E}_{out}$)	$-\rho_n \, q_n \, C_{p_n}(T_{n_{(z2)}} - T_\infty) \, \pi \, R^2$	$-\rho_n \, q_n \, C_{p_n}(T_{n_{(z=L)}} - T_\infty)\pi \, R^2$	(31)
Canola oil pyrolysis ($\dot{E}_{pyr}$)	$\int_{z1}^{z2} \Delta H_p(\phi S_w \rho_w) \, R_p \, \pi \, R^2 \, dz$	$\int_0^L \Delta H_p(\phi S_w \rho_w) \, R_p \, \pi \, R^2 \, dz$	(32)
Char oxidation ($\dot{E}_{oxi}$)	$\int_{z1}^{z2} \Delta H_c(\phi S_w \rho_w) \, R_c \, \pi \, R^2 \, dz$	$\int_0^L \Delta H_c(\phi S_w \rho_w) \, R_c \, \pi \, R^2 \, dz$	(33)
Radial heat loss ($\dot{E}_{loss}$)	$\int_{z1}^{z2} -U \, (T_w - T_\infty)2 \, \pi \, R \, dz$	$\int_0^L -U \, (T_w - T_\infty)2 \, \pi \, R \, dz$	(34)
Net ($\dot{E}_{net}$)	$\dot{E}_{in} + \dot{E}_{oxid} - \dot{E}_{out} - \dot{E}_{loss}$	$\dot{E}_{in} + \dot{E}_{oxid} - \dot{E}_{out} - \dot{E}_{loss}$	(35)

velocities ($\nu_f = 0.41 \pm 0.01$ cm min^{-1}) that progressed up to 46 cm until Dt = 1.32; however, after this height, the peak temperatures dropped until all fuel was fully consumed at 53 cm. Note that the initial packed fuel bed was 41 cm tall (i.e., which the smouldering front reached Dt = 1.00).

The results (Fig. 3a) during Dt > 1.00 correspond to smouldering propagation in the originally clean top sand pack that was impacted by fuel mobility. In other words, 19 % of canola oil mass (i.e., 118 g of the 637 g added) was mobilized up to the clean sand cap due to upward fuel mobility and smouldering propagated up to 12 cm in the newly contaminated fuel bed.

To minimize fuel mobility and better represent smouldering high viscous organic liquid waste (e.g., oil sludge), VI improver was added to canola oil at a mass ratio of 1:1 (Fig. 3b, c). The temperature-dependent viscosity of the homogeneous mixture increased by 19 times, agreeing with [15]. Experimental results of canola oil with VI improver (Exp. #*ii-iii*) show that, by increasing the viscosity of the fuel, more robust smouldering was achieved with higher $\nu_f = 0.52$ cm min^{-1} and $T_p = 570$ °C. Experimental results confirmed self-sustaining smouldering until $z = 41$ cm (i.e., the initial fuel bed height).

However, after this height, experimental extinction was achieved at $z = 42.5$ cm for $q_{n,in} = 0.025$ m s^{-1}, but smouldering remained self-sustained for $q_{n,in} = 0.062$ m s^{-1}. Altogether, upward fuel mobilization was minimized with the addition of VI improver.

Fig. 3d shows that, by increasing $q_{n,in}$ from 0.025 to 0.062 m s^{-1}, the experimental T_p was nearly constant around 570 °C; however, the smouldering front velocity (ν_f) increased from 0.45 to 0.52 cm min^{-1}. That shows the front velocities are more sensitive to air flux, where a 2.5 × increase in air flux has a much stronger impact than a 19 × increase in the fuel viscosity. Therefore, this analysis shows that, with sufficiently high Darcy air fluxes, the front velocity is not sensitive to the fuel viscosity. The trends in Fig. 3d are routinely found in applied smouldering studies [14,58-61].

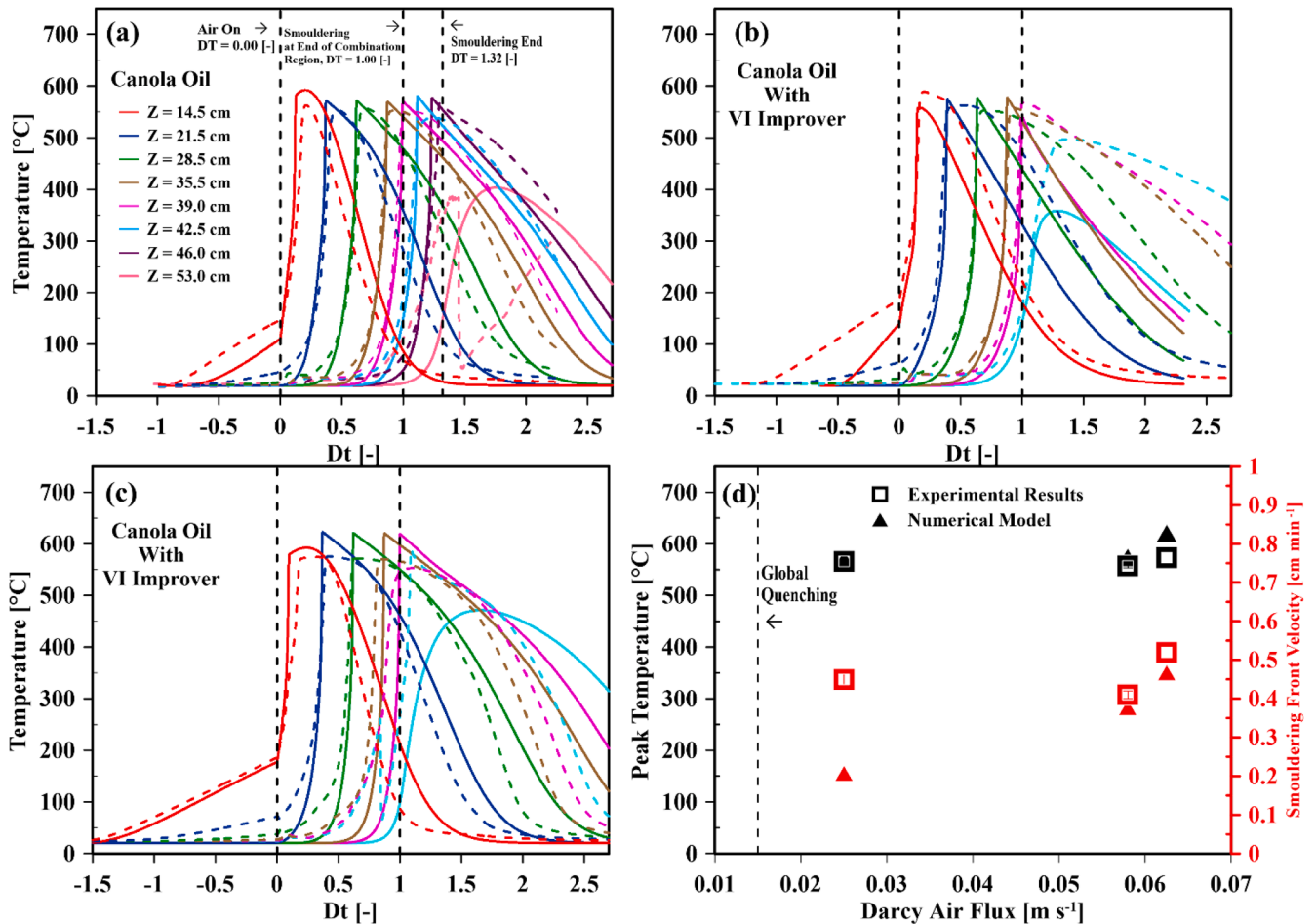The model was calibrated by adjusting the chemistry parameters ν_c,

Fig. 3. Temperature evolutions comparing experimental (dashed lines) and numerical (solid lines) results for: (a) canola oil at Darcy air flux (u_g) equal to 0.058 m s^{-1}; (b) and (c) canola oil with VI improver at Darcy air fluxes of 0.025 and 0.062 m s^{-1}, respectively; (d) shows the experimental and numerical smouldering front velocities (ν_f) and peak temperatures (T_p).

ν_{O_2}, ΔH_c, and ΔH_p to match experimental data from smouldering canola oil, following the methodology provided in [25]. This calibration was necessary as these parameters can change with process conditions due to the complex nature of smouldering chemistry [23]. These parameters are assumed consistent for canola oil: VI improver, as there is no significant deviation in heat release pattern (e.g., as observed in the peak temperatures).

The calibrated model results in Fig. 3a show good agreement with experimental data, with the temperatures errors near 8 %, calculated via the methodology from [24]. The numerical ν_f and T_p at these calibrated conditions were 0.37 cm min^{-1} and 574 °C, respectively, which match well with experimental results (Fig. 3d).

Figs. 3b and 3c show the robustness of the calibrated model in predicting independent experimental results (Exp. # ii-iii, Table 1) conducted using canola oil with VI improver at two different $q_{n,in}$ (i.e., 0.025 and 0.062 m s^{-1}). The calibrated model accurately predicted the key experimental metrics, i.e., ignition temperature (360 °C), T_p (620 °C), and ν_f (0.46 cm min^{-1}) with an average error of 14 %. The deviation of ν_f is hypothesized to result from fuel downward mobility from the pre-heating zone to the reaction zone due to low air pressure gradients. It appears that additional dynamics emerge under these conditions in the experiments, which were not fully captured within the model assumptions. For example, the deviations between experimental and modelled ν_f may be due to multi-dimensional or phase change effects that were not included in this work. Moreover, the model predicted upward fuel mobility in low and high $q_{n,in}$, where smouldering was extinct at $z = 42.5$ cm. This is the first-time fuel mobility has been simulated in applied smouldering systems. It is hypothesized that temperature difference between model and experiments in this region is associated with uncertainties due to upward fuel mobilization, boundary effects, and fuel evaporation-condensation that was not considered in the model.

The experiments and simulations with pure VI improver (i.e., $\mu_w = 31.04$ Pa s at ambient temperature, which represents no mobility) at two different Darcy air fluxes of 0.025 and 0.062 m s^{-1} confirm almost uniform T_p and ν_f. Therefore, these results demonstrate that fuels with ambient viscosities higher than 1.33 Pa s do not exhibit noticeable mobility effects (see Supplementary Material, Section B).

These results demonstrate the model validation at different experimental conditions without further calibration. Overall, the model reproduced key experimental trends that govern the complex interplay between coupled heat and mass transfer, multi-phase flow, and chemical reactions in these smouldering experiments with different fuel viscosities, saturations, and air fluxes.

3.2. Mobility versus non-mobility

Fig. 4a shows a comparison between smouldering numerical simulations using: (i) canola oil (i.e., with mobility due to canola oil's low μ_w of 0.07 Pa s at 20 °C, Simulation # 1) and (ii) VI improver (i.e., effectively without mobility due to pure VI improver's high $\mu_w = 31.04$ Pa s at 20 °C, Simulation # 4). These results demonstrate that, without mobility, smouldering progressed more robustly with a higher average $T_p = 662$ °C and $\nu_f = 0.46$ cm min^{-1}.

Fig. 4b shows saturation histories at different positions in the simulation from smouldering canola oil (solid lines) and VI improver (dotted lines) with the initial saturation ($S_{w,0}$) = 0.30. The canola oil simulations show downward mobilization with a decrease in S_w during the air-off period at positions (i) near the heater, where temperature effects on the canola oil viscosity were high (i.e., at $z = 14.5$ cm, S_w decreased from 0.30 to 0.20), and (ii) at the top of the fuel bed due to gravity (i.e., at $z = 35.5$ cm, S_w decreased from 0.30 to 0.22). Conversely, VI improver did not migrate during the air-off period and S_w remained unchanged.

Upon smouldering ignition, changes in temperature distributions and upward forces associate with air pressure gradients caused further canola oil redistribution. This pressure redistribution is illustrated in Fig. 5e, where the main trends agree strongly with routine experimental observations [62]. For example, mobile fuel is routinely found in the initially clean sand caps in experiments as documented in [15,21]. As smouldering progressed, the canola oil was pushed ahead of the chemical reactions. Fig. 4b shows that this accumulation of canola oil by progressing the smouldering front increased the magnitude and location of the peak saturation ($S_{w,peak}$) from 0.23 to 0.53 at $z = 14.5$ to 35.5 cm, respectively. When the smouldering front reached the top of the fuel bed, canola oil was pushed into the initially clean sand and the final $S_{w,peak}$ values decreased to 0.36 at $z = 46.0$ cm. The canola oil was finally consumed at $z = 53$ cm (see Fig. 3a). Conversely, the VI improver saturation was constant ahead of the smouldering front over time. That is, the VI improver saturation was either 0.30 (i.e., before smouldering) or 0.00 (i.e., after smouldering), agreeing with [21,61,63]. The results for VI improver therefore represent typical smouldering using non-mobile fuel. Overall, the model results provide previously unknown insights into the effects of fuel mobility on temperature and saturation distributions.

3.3. Dynamics of mobility

To better understand the dynamics of fuel mobility in smouldering systems, Fig. 5 presents the distributions of different parameters including canola oil temperature (T_w), saturation (S_w), oxygen mass
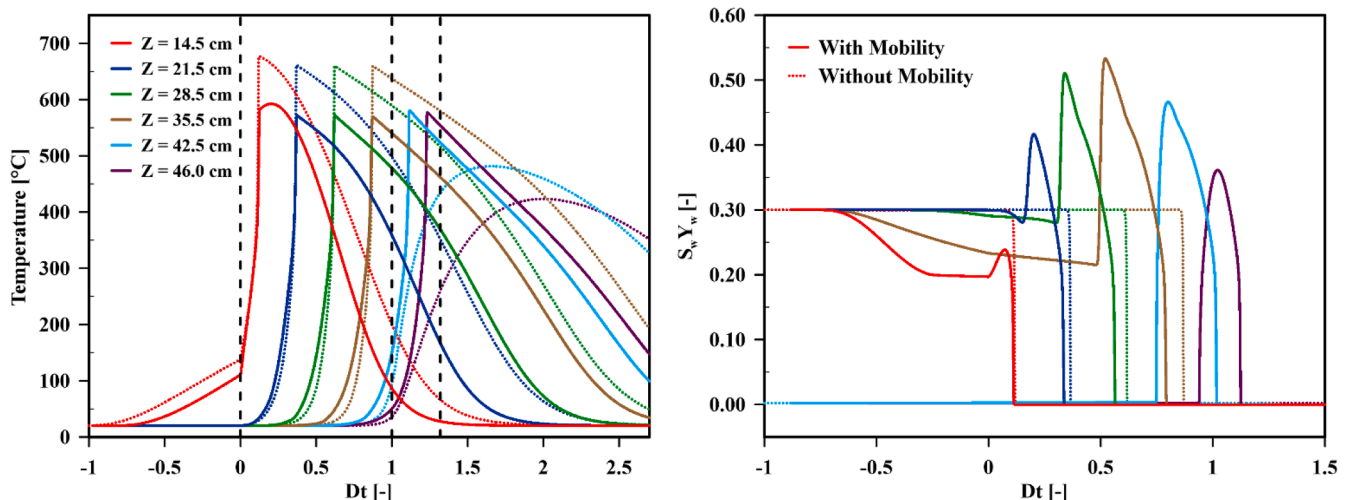

Fig. 4. (a and b) numerical simulation of temperature evolution comparing canola oil (solid lines) and VI improver for $q_{n,in} = 0.058$ m s^{-1} (dotted lines).
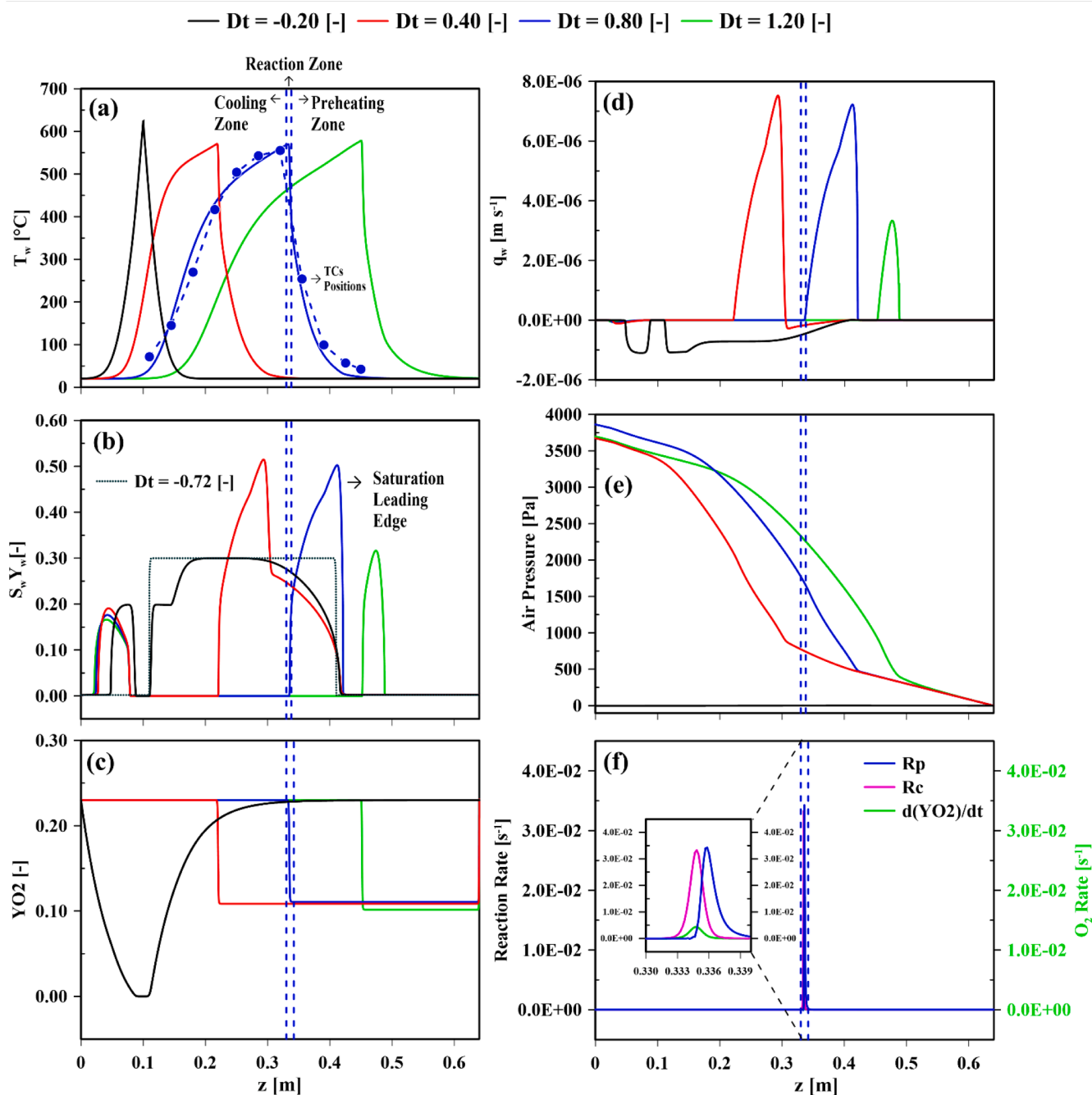
Fig. 5. Distribution of various key parameters for the base simulation (canola oil): (a) temperature (T_w), (b) saturation (S_w), (c) oxygen mass fraction (Y_{O2}), (d) Darcy flux of canola oil (q_w), (e) air pressure (P_n), (f) reaction rates at Dt = 0.80 (R_p and R_c) and oxygen consumption rate (dY_{O2}/dt), at four different times: Dt = −0.20, 0.40, 0.80, and 1.20. Dashed vertical blue lines show the position of reaction zone at Dt = 0.80.

fraction (Y_{O2}), Darcy flux of canola oil (q_w), air pressure (P_n), and reaction rates (R) at different times (Dt = −0.20, 0.40, 0.80, 1.20).

At Dt = 0, canola oil was at an initial saturation of 0.30 while the entire domain was at ambient temperature (i.e., 20 °C). The heater was turned on during the preheating period (e.g., at Dt = −0.20), when $T_{w,peak}$ increased to 620 °C (Fig. 5a) and canola oil migrated downward to the initially clean sand region below the heater due to gravity forces (Fig. 5b, confirmed with $q_w < 0$). Weak oxidation reactions resulted from the initial oxygen in the pores, which was depleted near the heater before ignition (Fig. 5c).

From 0.00 < Dt < 1.00, the smouldering front progressed through fuel bed with consistent $T_p = 570$ °C (Fig. 5a); however, $S_{w,peak}$ increased up to 0.51 (Fig. 5b) due to fuel accumulation in the preheating zone. For

example, at Dt = 0.40 (smouldering front position at z = 0.22 m), canola oil was pushed upward ($q_w > 0$ m s^{-1}, Fig. 5d) in the preheating zone due to air pressure gradient forces (Fig. 5e), which decreased the saturation in the reaction zone ($S_w = 0.23$). This mobility ultimately decreased T_p, compared to high viscous fuel with minimal mobility (see Fig. 4a). Above the preheating zone, canola oil was at ambient temperature where gravity dominated downward mobility and S_w decreased to 0.27 ($S_{w,0} = 0.30$). At this time, the pressure at the bottom of the reactor increased to 3.7 kPa (Fig. 5e).

At Dt = 0.80, the cooling zone grew; therefore, the overall pressure drop across the system increased over time, due to the increased flow resistance from the high temperature and high viscosity air [62], and the peak pressure at reactor base increased to 3.9 kPa. In addition, the

relative air permeability (k_{rn}) decreased in preheating zone due to fuel accumulation, which increased the pressure drop across this zone. This increasing pressure trend is common across applied smouldering systems with a constant air mass flux [48,49]. Moreover, the reaction zone shows that the two-step canola oil pyrolysis and char oxidation took place within a thin, ~7.0 mm region that coincided with the peak temperature and maximum oxygen consumption rate ($dY_{O2}/dt = 0.004$ [s^{-1}]). This thin reaction zone is commonly observed in many comparable smouldering systems [61,64,65].

At Dt > 1.00 (e.g., Dt = 1.20), a slightly higher oxygen mass fraction (Y_{O2}) was consumed and T_p increased slightly as the smouldering front accelerated due to end-effects. However, $S_{w,peak}$ decreased as fuel was consumed by the front, which resulted in decreasing q_w (i.e., from 7.2 to 3.3×10^{-6} m s^{-1}) associated with decreasing relative canola oil permeability (k_{rw}) (see Eq. (14) and 16). After smouldering reached the top of the reactor ($z = 53$ cm), all canola oil was consumed and only hot clean sand remained.

Overall, Fig. 5 illustrates many key dynamics of fuel mobility in applied smouldering systems, where the modelled temperatures along the height of the column aligned well with experimental observations (Fig. 5a). These results provide critical insight and clarity into the key mobility trends routinely observed in liquid fuel smouldering experiments and applications.

3.4. Sensitivity analysis

Fig. 6 and 7 illustrate the sensitivity analysis of inlet Darcy air flux ($q_{n,in}$), initial saturation ($S_{w,0}$), intrinsic permeability (k_i), fuel viscosity (μ_w), pore size distribution index (λ), and the fuel bed length (L) on T_w, S_w, Y_{O2} distributions, and T_p and ν_f at Dt = 0.50.

3.4.1. Inlet darcy air flux ($q_{n,in}$)

Darcy air flux ($q_{n,in}$) is one of the most effective parameters in controlling smouldering characteristics (e.g., robustness, T_p, and ν_f) and fuel mobility, as it causes increasing air pressure gradients. All scenarios in Table 1 show that by increasing $q_{n,in}$ from 0.040 to 0.080 m s^{-1} (in Simulation # 5 to 6, respectively): (*i*) the saturation leading edge

position progressed from $z = 0.28$ to $z = 0.36$ m, respectively, due to higher air pressure gradient forces; (*ii*) a lower Y_{O2} was consumed due to increased $\rho_n q_{n,in} Y_{O2}$ delivered to the front (see Fig. 6a, b); and (*iii*) ν_f increased from 0.32 to 0.44 cm min^{-1}, respectively. However, T_p and fuel mobilization below the heater during the air-off period remained almost constant, i.e., 575 ± 6 °C, $S_w = 0.18$ (see Fig. 7a).

With a low $q_{n,in} = 0.025$ m s^{-1}, T_p increased to 625 °C (i.e., relative to 575 °C at 0.040 m s^{-1}), while ν_f decreased to 0.20 cm min^{-1} (i.e., relative to 0.28 cm min^{-1} at 0.040 m s^{-1}). While the ν_f trend is expected, the T_p trend is not. Both trends reflect that, by decreasing $q_{n,in}$, more fuel was mobilized into the reaction zone, which resulted in higher T_p, agreeing with [15,66]. This redistribution is a key phenomenon unique to mobile liquid fuels. That is, this effect is not seen in smouldering immobile fuels (e.g., GAC) [25]. Fig. 7a also shows that, with a very low $q_{n,in} = 0.015$ m s^{-1}, smouldering was not self-sustaining, as the radial heat losses dominated over the produced oxidation energy and the global net energy rate was negative (see further discussion in Section 3.5).

3.4.2. Initial saturation ($S_{w,0}$)

Fig. 6c shows that by increasing $S_{w,0}$ from 0.20 to 0.40 (in Simulation # 8 to 9, respectively), more fuel was mobilized downward below the heater during the air-off period ($S_w = 0.25$ for $S_{w,0} = 0.40$). T_p and oxygen consumption (ΔY_{O2}) remained uniform ($T_p = 570$ °C, $\Delta Y_{O2} = 12$ %) in comparison to the base case ($T_p = 574$ °C, $\Delta Y_{O2} = 12$ %), which shows that – in this saturation range – nearly the same amount of fuel was consumed in the reaction zone. This finding qualitatively agrees with Section 3.4.6 and experimental data from [67], which both hypothesize that a high $q_{n,in} = 0.058$ m s^{-1} caused sufficient upward air pressure gradient force to drive the fuel into the preheating zone (i.e., ahead of the smouldering front). In these conditions, no fuel leaked from preheating zone to the reaction zone. The ν_f slightly dropped (i.e., from 0.38 to 0.35 cm min^{-1}) due to fuel accumulation in the preheating zone, which also decreased the relative air permeability (k_{rn}) and Darcy air flux (q_n).

Fig. 7b confirms that by decreasing the saturation below 0.20, both T_p and ν_f dropped, as lower S_w was deposited in the reaction zone and smouldering became weak. For $S_w < 0.05$, smouldering was not self-
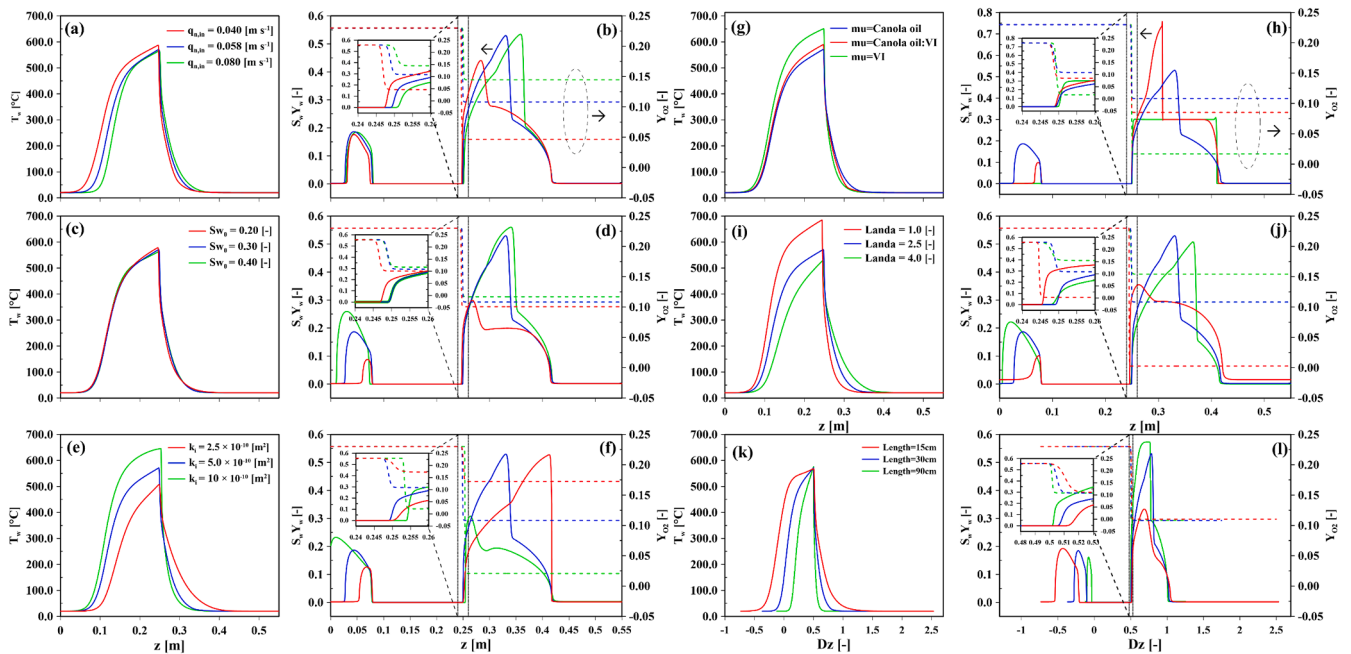

Fig. 6. Sensitivity analysis at Dt = 0.5 of (a, b) inlet Darcy air flux ($q_{n,in}$), (c, d) initial saturation (S_{w0}), (e, f) intrinsic permeability (k_i), (g, h) fuel viscosity (μ), (i, j) pore size distribution index (λ), and (k, l) contamination length (L) on temperature (T_w), fuel saturation ($S_w Y_w$), and oxygen mass fraction (Y_{O2}) distribution dynamics in the reactor.
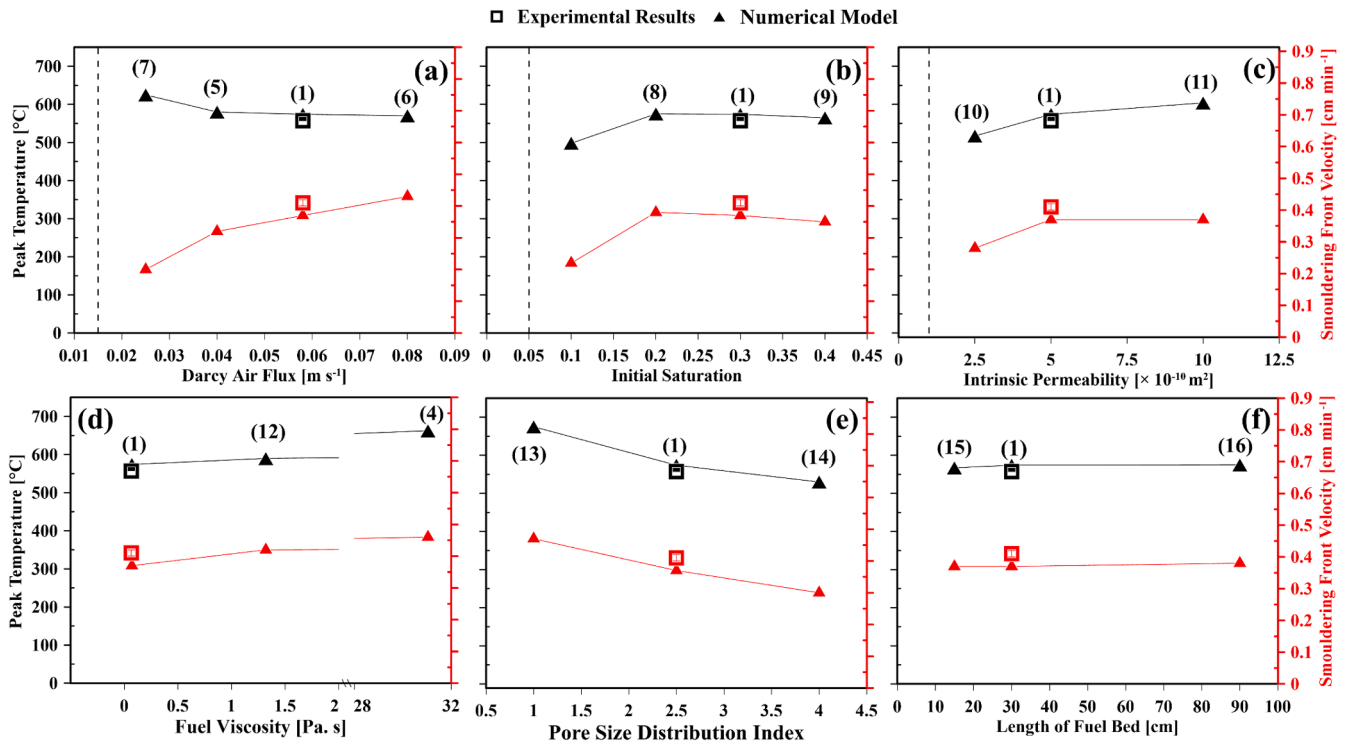
Fig. 7. Sensitivity analyses of (a) inlet Darcy air flux ($q_{n,in}$), (b) initial saturation ($S_{w,0}$), (c) intrinsic permeability (k_i), (d) fuel viscosity (μ), (e) pore size distribution index (λ), and (f) fuel bed length (L) on peak temperatures (T_p) and smouldering front velocities (ν_f). The parenthesis numbers indicate the simulation # in Table 1.

sustaining as energy losses overwhelmed the oxidation energy production rate (see additional discussion in Section 3.5).

3.4.3. Intrinsic permeability (k_i)

Fig. 6e shows key sensitivities to intrinsic permeability (k_i). When k_i was halved (i.e., from $k_i = 5$ to 2.5×10^{-10} m² in Simulation # 1 to 10, respectively), less fuel was mobilized downward below the heater during the air-off period ($S_w = 0.12$ vs. $S_w = 0.19$, respectively). Moreover, the saturation leading edge in the low k_i Simulation # 10 was located at $z = 41$ cm (base case, $z = 33$ cm), which indicates that upward fuel mobilization carried a large fraction of fuel further ahead into the preheating zone. This upward mobilization resulted in less fuel deposited in the reaction zone, where the deposited S_w decreased from 0.23 (base case) to 0.15. This decreased saturation deteriorated the reaction robustness $T_p = 506$ °C and $\nu_f = 0.28$ cm min⁻¹ (relative to base case values: $T_p = 574$ °C and $\nu_f = 0.37$ cm min⁻¹). Ultimately, these effects were due to a large upward air pressure gradient forces against downward gravity, driven by higher air pressures in the low k_i Simulation # 10. Conversely, doubling k_i (i.e., from $k_i = 5$ to 10×10^{-10} m² in Simulation # 1 to 11, respectively) increased downward mobilization during air-off period and lowered upward fuel mobilization (i.e., as the saturation leading edge was located close to the reaction zone at $z = 0.29$ m). Thus, more fuel was deposited in the reaction zone, i.e., S_w increased from 0.23 (base case) to 0.27 (high k_i Simulation # 11). This S_w increase resulted in a high $T_p = 645$ °C and increased oxygen consumption (final Y_{O2} from 0.11 to 0.02), relative to the base case (Simulation # 1).

3.4.4. Temperature-dependent viscosity of fuel (μ_w)

Fig. 6g illustrates the effects of μ_w on T_w and S_w distributions for three different fuels: (*i*) Canola oil (Simulation # 1, base case simulation), (*ii*) Canola oil with VI at a mass ratio of 1:1 (i.e., Simulation # 12), and (*iii*) VI improver-only (i.e., Simulation # 4). For (*i*), μ_w decreased from 0.070 to 0.009 Pa s when temperature increased from ambient (20 °C) to ignition temperature (360 °C), respectively. This temperature dependency strongly affects fuel downward mobilization below the heater during the

air-off period and upward mobilization to the preheating zone. Downward mobilization resulted in $S_w = 0.19$ below the heater.

For (*ii*), the addition of VI in the canola oil increased μ_w to 1.32 Pa s (ambient temperature) and 0.017 Pa s (ignition temperature), i.e., approximately 19 and 2 times more viscous than canola oil alone at the respective temperatures. Practically, these higher viscosities resulted in a slight downward mobilization below the heater during the air-off period. However, upward mobility was the highest in the preheating zone reaching $S_w = 0.75$ at $z = 0.30$. Slightly more fuel ($S_w = 0.24$) remained in the reaction zone when compared to the base case and resulted in $T_p = 590$ °C and $\nu_f = 0.42$ cm min⁻¹. Between $z = 0.31$ and $z = 0.39$, saturation distribution remained uniform ($S_w = 0.30$), as this region experienced near-ambient temperatures with the high viscosity fuel.

For (*iii*), μ_w increased to 31.04 (ambient temperature) and 5.00 Pa s (ignition temperature), i.e., 444 and 556 times more viscous than canola oil at the respective temperatures. Downward and upward mobility were not observed due to VI's high viscosity. Therefore, S_w remained uniform as smouldering progressed to the top of the reactor. In this case, the smouldering front consumed the entire fuel (i.e., $S_w = 0.30$) in the reaction zone, which resulted in the highest $T_p = 650$ °C (see Fig. 7d), and greatest oxygen consumption (final $Y_{O2} = 0.11$ to 0.01)

3.4.5. Pore size distribution index

Fig. 6i and j illustrate the effects of λ on T_w and S_w distribution in the reactor. $\lambda = 2.5$ represents a normal pore size distribution performed in the base case simulation, while a lower $\lambda = 1$ represents wider pore size distribution (i.e., poorly sorted material such as highly heterogeneous soil), and a higher $\lambda = 4$ represents a narrower pore size distribution (i.e., well-sorted material such as glass beads, see Eq. (12)). By decreasing λ to 1 (Simulation # 13), downward and upward fuel mobilization were limited, as gravity and air pressure gradient forces were less effective; therefore, more fuel ($S_w = 0.32$) was concentrated in the reaction zone than the base case Simulation # 1 ($S_w = 0.23$), which caused higher $T_p = 675$ °C, and faster $\nu_f = 0.47$ cm min⁻¹, with entire oxygen

consumption, relative to the base case ($\Delta Y_{O2} = 0.12$). This is the only scenario in which S_w was concentrated in the reaction zone more than $S_{w,0}$ and oxygen was entirely consumed. By increasing λ to 4 (Simulation #14), fuel easily migrated through the porous medium, which resulted in more fuel mobilization below the heater during the air-off period and in the preheating zone away from the reaction zone (i.e., only $S_w = 0.13$ remained in the reaction zone). Therefore, T_p and ν_f decreased to 527 °C and 0.30 cm min^{-1}, respectively, relative to the base case ($T_p = 574$ °C, and $\nu_f = 0.37$ cm min^{-1}). As λ and displacement pressure (P_d) are interconnected, a sensitivity on P_d was performed in Supplementary Material, Appendix C.

3.4.6. Fuel bed length (L)

Fig. 6k and l illustrate the effects of L on T_w and S_w distributions. Decreasing L from 30 (base case Simulation # 1) to 15 cm (Simulation #15), decreased the peak saturation ($S_{w,peak}$) to 0.33 (in comparison to 0.53 in the base case), and T_p to 567 °C (compared to 574 °C in the base case) as less fuel remained in the reaction zone due to mobility ($S_w = 0.15$). However, ν_f (0.37 cm min^{-1}) and oxygen consumption were nearly the same as the base case. These simulations showed that, by decreasing L, a comparable amount of fuel was mobilized downward below the heater during air-off period. Moreover, $S_{w,peak}$ decreased; however, almost uniform ν_f with the base case was achieved.

By increasing L to 90 cm (Simulation # 17), canola oil accumulated in the preheating zone and $S_{w,peak}$ increased to 0.57; however, T_p was nearly the same as the base case, as deposited S_w in the reaction zone remained uniform. This finding is consistent with the experimental results from [15] where high $q_{n,\ in}$ prevented fuel migration from the preheating zone to the reaction zone, which moderated the T_p.

Overall, Section 3.5 presents the results from the sensitivity analysis that showed how key system parameters affected smouldering performance. These results show that higher T_p, ν_f, and Y_{O2} consumption were all associated with conditions that led to higher fuel saturations in the reaction zone, which in turn led to more robust oxidation reactions (see Section 3.5).

3.5. Sensitivity of energy analysis

To verify the model and quantify the effects of liquid mobility on smouldering systems, local (i.e., across the smouldering front) and global (i.e., across the entire system) energy analyses were conducted for the cases presented in Section 3.4 at Dt =0.5 (see Supplementary Material, Section D). In all the cases for the local energy balance, oxidation energy rate ($\dot{E}_{oxid}$) mostly contributed to the net energy rate ($\dot{E}_{net}$), while the inlet and outlet energy rates nearly balanced (i.e., energy delivered to and from the reaction zone by the convective heat flux of air, $\dot{E}_{in}$, and $\dot{E}_{out}$, respectively). In global energy balance, $\dot{E}_{in}$ (i.e., energy delivered from heater) and $\dot{E}_{out}$ (i.e., energy convected by hot air at the top of the reactor) did not impact the global energy balance in any case, as the analysis was performed in the middle of smouldering propagation, when the system was not affected by initial- or end-effects, respectively. By increasing $q_{n,in}$, local $\dot{E}_{out}$ increased, which promoted pyrolysis and oxidation reactions and increased ν_f (see Fig. 7a). However, due to decreased S_w remaining in the reaction zone during upwards mobility, $\dot{E}_{oxid}$ and $\dot{E}_{Pyr}$ decreased (see Fig. 6b).

Fig. 8c shows the minimal local energy rate changes by increasing $S_{w,0}$ from 0.20 to 0.40. A previous study showed that, without the effect of mobility, $\dot{E}_{oxid}$ increased linearly with $S_{w,0}$, which resulted in higher T_p and $\dot{E}_{out}$ [14]. However, by considering the effect of mobility and a relatively high $q_{n,in} = 0.058$ m s^{-1}, the fuel mobilized upward away from reactions into the preheating zone. Therefore, the S_w in the reaction zone

was nearly constant in both $S_{w,0} = 0.20$ and 0.40 cases and, consequently, the $\dot{E}_{oxid}$ and T_p were also nearly constant. Similar behaviour was found in the global energy balance (Fig. 8d).

Fig. 8e shows that by increasing k_i, more S_w remained in the reaction zone; therefore, $\dot{E}_{oxid}$ and T_p increased and more energy was convected ($\dot{E}_{out}$) to the virgin fuel in the preheating zone, which provided more energy for pyrolysis ($\dot{E}_{pyr}$). Similar behaviour was found in the global energy balance, Fig. 8f.

Fig. 8g shows the effects on the local energy balance from increasing the fuel bed from 15 to 90 cm, which fostered more fuel accumulation in the preheating zone, as the front took longer to reach the middle of the fuel bed in the taller system. The $\dot{E}_{oxid}$ increased slightly as higher S_w remained in the reaction zone; however, ν_f remained nearly uniform across all L cases. Fig. 8h confirms that the global $\dot{E}_{net}$ decreased with increasing L, which was expected because taller systems exhibit growing contributions of heat losses from longer cooling zones in a taller system. Therefore, the overall system robustness remained almost uniform for these systems with varying lengths.

Overall, these analyses reveal the impacts of key fuel mobility sensitivities on smouldering systems' energy balances. Moreover, this energy analysis confirms the prominent role of mobility in determining the system robustness, i.e., by decreasing S_w within the reaction zone due to mobility, the $\dot{E}_{oxid}$, $\dot{E}_{net}$, and system robustness also decreased.

4. Conclusion

In this study, a previously developed 1D numerical model was equipped with multiphase flow equations, calibrated with experiments using canola oil (low viscosity, highly mobile), and validated with experiments using canola oil mixed with VI improver (medium viscosity, moderately mobile) and VI improver alone (high viscosity, non-mobile).

The model was capable of predicting experimental results in terms of temperature histories and smouldering front velocities for many conditions beyond those used for calibration. Accurate predictions of these two variables served to provide sufficient confidence that the model was reproducing the key smouldering features. The model was then used to extract information that cannot be readily measured experimentally.

A higher peak temperature and smouldering front velocity was achieved with the non-mobile fuel as higher fuel remained in the reaction zone and less fuel was moved upward into the preheating zone.

A sensitivity analysis was performed to understand the effects of saturation, viscosity, Darcy air flux, intrinsic permeability, and pore size distribution index on saturation distribution, peak temperature, front velocity, and oxygen consumption. In all scenarios, fuel saturation distribution was affected. Fuel viscosity, porous medium permeability, and pore size distribution index had the strongest impacts on temperatures.

Local and global analyses were conducted to quantify the effects of mobility on the system energy balance. The oxidation energy rate was highly dependent on saturation of fuel within the reaction zone and was affected by fuel, porous medium, and air flux characteristics. In all cases with a sufficiently high Darcy air flux, negligible fuel saturation leaked from the preheating zone into the reaction zone. Therefore, oxidation energy rate and system robustness mainly depended on the initial fuel deposition and smouldering front velocity.

Altogether this study provides novel insight into key fuel mobility dynamics that often affect applied smouldering systems. Many dynamics have not been previously investigated. The insight provided from this study will provide engineers and researchers with new information to design improved applied smouldering systems for environmentally beneficial purposes.
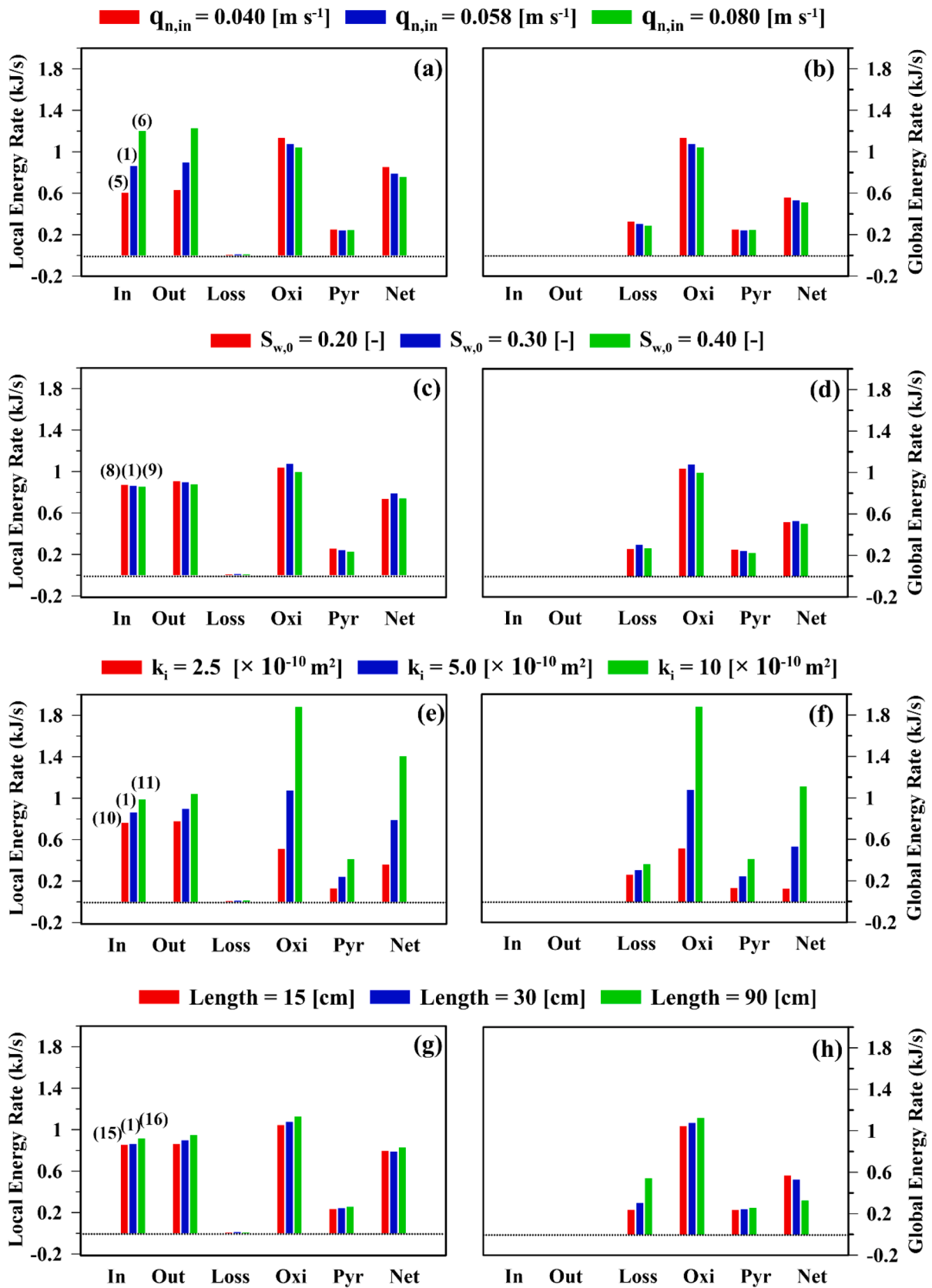
Fig. 8. Local and global energy rates for oxidation ($\dot{E}_{oxid}$), loss ($\dot{E}_{loss}$), inlet ($\dot{E}_{in}$), outlet ($\dot{E}_{out}$), and their net results ($\dot{E}_{net}$) at Dt = 0.5 [-]. The parenthesis numbers indicate the simulation # in Table 1.

Novelty and significance statement

Applied smouldering systems are gaining popularity as a novel means to treat organic liquid waste. However, these systems often experience liquid mobility, which can lead to operational problems. Liquid mobility in this context is poorly understood. This study bridges a key knowledge gap in understanding the dynamics of organic liquid mobilization in these systems using numerical modelling. The model's ability to predict temperature histories and smouldering front velocities with high accuracy establishes a reliable tool for sensitivity analyses over a range of system operating conditions. This research clarifies how higher viscosity fuels can enhance smouldering efficiencies by retaining more fuel in the reaction zone. This study contributes to advancing the design and implementation of smouldering-based systems for environmentally beneficial applications.

CRediT authorship contribution statement

Seyed Ziaedin Miry: Writing – original draft, Validation, Methodology, Investigation, Formal analysis, Data curation, Conceptualization. **Marco A.B. Zanoni:** Writing – review & editing, Software, Methodology, Investigation, Formal analysis, Conceptualization. **Tarek L. Rashwan:** Writing – review & editing, Supervision, Methodology, Investigation, Data curation, Conceptualization. **Laura Kinsman:** Writing – review & editing, Validation, Investigation. **José L. Torero:** Writing – review & editing, Validation, Supervision, Project administration, Investigation, Formal analysis, Conceptualization. **Jason I. Gerhard:** Validation, Supervision, Resources, Project administration, Funding acquisition, Formal analysis, Conceptualization.

Declaration of competing interest

The authors declare the following financial interests/personal relationships which may be considered as potential competing interests:

Geosyntec Consultants, through its subsidiary Savron, holds an exclusive license to commercialize the smouldering remediation technology. Laura Kinsman is employed by and a shareholder in Geosyntec Consultants, Inc. If there are other authors, they declare that they have no known competing financial interests or personal relationships that could have appeared to influence the work reported in this paper.

Acknowledgements

Supplementary materials

Supplementary material associated with this article can be found, in the online version, at doi:10.1016/j.combustflame.2024.113789.

References

[1] Z. Gan, C. Zhao, Y. Li, G. Chen, Z. Song, Z. Zhang, W. Ran, Experimental investigation on smoldering combustion for oil sludge treatment: influence of key parameters and product analysis, Fuel 316 (2022) 123354.

[2] C. Zhao, Y. Li, Z. Gan, M. Nie, Method of smoldering combustion for refinery oil sludge treatment, J. Hazard. Mater. 409 (2021) 124995.

[3] J.E. Vidonish, K. Zygourakis, C.A. Masiello, G. Sabadell, P.J. Alvarez, Thermal treatment of hydrocarbon-impacted soils: a review of technology innovation for sustainable remediation, Engineering 2 (2016) 426–437.

[4] D. Czajczyńska, L. Anguilano, H. Ghazal, R. Krzyżyńska, A. Reynolds, N. Spencer, H. Jouhara, Potential of pyrolysis processes in the waste management sector, Thermal Sci. Eng. Progress 3 (2017) 171–197.

[5] S.M. Frolov, Organic waste gasification: a selective review, Fuels 2 (2021) 556–650.

[6] N. Jurado, T. Somorin, A.J. Kolios, S. Wagland, K. Patchigolla, B. Fidalgo, A. Parker, E. McAdam, L. Williams, S. Tyrrel, Design and commissioning of a multi-mode prototype for thermochemical conversion of human faeces, Energy Convers. Manage. 163 (2018) 507–524.

[7] Y.B. Yang, A.N. Phan, C. Ryu, V. Sharifi, J. Swithenbank, Mathematical modelling of slow pyrolysis of segregated solid wastes in a packed-bed pyrolyser, Fuel 86 (2007) 169–180.

[8] H.K. Wyn, M. Konarova, J. Beltramini, G. Perkins, L. Yermán, Self-sustaining smouldering combustion of waste: a review on applications, key parameters and potential resource recovery, Fuel Process. Technol. 205 (2020) 106425.

[9] X. Wang, S. Deng, H. Tan, A. Adeosun, M. Vujanović, F. Yang, N. Duić, Synergetic effect of sewage sludge and biomass co-pyrolysis: a combined study in thermogravimetric analyzer and a fixed bed reactor, Energy Convers. Manage. 118 (2016) 399–405.

[10] M. Toledo, N. Ripoll, J. Céspedes, A. Zbogar-Rasic, N. Fedorova, V. Jovicic, A. Delgado, Syngas production from waste tires using a hybrid filtration reactor under different gasifier agents, Energy Convers. Manage. 172 (2018) 381–390.

[11] R. Pan, G. Debenest, Numerical investigation of a novel smoldering-driven reactor for plastic waste pyrolysis, Energy Convers. Manage. 257 (2022) 115439.

[12] A.W. Sims, G.P. Sabadell, C.W. Lam, D.C. Segal, P. Bireta, D. Thomas, Self-sustaining smouldering combustion for the treatment of industrial oily waste, Waste Manage. Res. (2022) 0734242X221123145.

[13] T.J. Ohlemiller, Modeling of smoldering combustion propagation, Prog. Energy Combust. Sci. 11 (1985) 277–310.

[14] M.A. Zanoni, J.L. Torero, J.I. Gerhard, Delineating and explaining the limits of self-sustained smouldering combustion, Combust. Flame 201 (2019) 78–92.

[15] L. Kinsman, J. Torero, J. Gerhard, Organic liquid mobility induced by smouldering remediation, J. Hazard. Mater. 325 (2017) 101–112.

[16] P.S. Sarathi, In-situ Combustion Handbook–Principles and Practices, National Energy Technology Lab.(NETL), Tulsa, OK (United States). National, 1999.

[17] J.D.M. Belgrave, R.G. Moore, M.G. Ursenbach, D.W. Bennion, A Comprehensive Approach to In-Situ Combustion Modeling, 4 (1993).

[18] K.H. Coats, In-situ combustion model, Soc. Petroleum Eng. J. 20 (1980) 533–554.

[19] M. Yang, T.G. Harding, Z. Chen, K. Yu, H. Liu, B. Yang, R. He, Numerical modelling of hybrid steam and in-situ combustion performance for oil sands, in: editorˆeditors. SPE Reservoir Simulation Conference, OnePetro, 2017 p.

[20] M. Ursenbach, R. Moore, S. Mehta, Air injection in heavy oil reservoirs-a process whose time has come (again), J. Can. Petroleum Technol. 49 (2010) 48–54.

[21] K. Aounallah, Efficient Simulation and Analysis of the Effects of Permeability on the In-Situ Combustion of Heavy Oils, in: editorˆeditors. SPE Annual Technical Conference and Exhibition, 2019.

[22] D.S. Reddya, G.S. Kumarb, A numerical investigation on the role of oil saturations on performance of in-situ combustion in porous media, Int. J. Scientif. T Eng. Res. 5 (2014) 531–538.

[23] J.L. Torero, J.I. Gerhard, M.F. Martins, M.A. Zanoni, T.L. Rashwan, J.K. Brown, Processes defining smouldering combustion: integrated review and synthesis, Prog. Energy Combust. Sci. 81 (2020) 100869.

[24] S.Z. Miry, M.A. Zanoni, T.L. Rashwan, J.L. Torero, J.I. Gerhard, Investigation of multi-dimensional transfer effects in applied smouldering systems: a 2D numerical modelling approach, Combust. Flame 246 (2022) 112385.

[25] S.Z. Miry, M.A. Zanoni, T.L. Rashwan, J.L. Torero, J.I. Gerhard, Investigation of applied smouldering in different conditions: the effect of oxygen mass flux, Fuel Process. Technol. 250 (2023) 107849.

[26] G. Rein, A. Bar-Ilan, A.C. Fernandez-Pello, J.L. Ellzey, J.L. Torero, D.L. Urban, Modeling of one-dimensional smoldering of polyurethane in microgravity conditions, Proc. Combust. Inst. 30 (2005) 2327–2334.

[27] G. Rein, A.Carlos Fernandez-Pello, D.L. Urban, Computational model of forward and opposed smoldering combustion in microgravity, Proc. Combust. Inst. 31 (2007) 2677–2684.

[28] G. Rein, C. Lautenberger, A.C. Fernandez-Pello, J.L. Torero, D.L. Urban, Application of genetic algorithms and thermogravimetry to determine the kinetics of polyurethane foam in smoldering combustion, Combust. Flame 146 (2006) 95–108.

[29] J. Yang, H. Chen, N. Liu, Heat loss and kinetic effects on extinction and critical self-sustained propagation of forced forward smoldering, in: editorˆeditors. Fire Science and Technology 2017, Springer, 2015, pp. 831–840.

[30] M.A. Zanoni, J.L. Torero, J.I. Gerhard, Determining the conditions that lead to self-sustained smouldering combustion by means of numerical modelling, Proc. Combust. Inst. 37 (2019) 4043–4051.

[31] J. Yang, H. Chen, N. Liu, Modeling of two-dimensional natural downward smoldering of peat, Energy Fuels. 30 (2016) 8765–8775.

[32] A. Rostami, J. Murthy, M. Hajaligol, Modeling of a smoldering carbonaceous rod, Fuel Chem. Div. Preprints (2002).

[33] A. Rostami, J. Murthy, M. Hajaligol, Modeling of a smoldering cigarette, J. Anal. Appl. Pyrolysis 66 (2003) 281–301.

[34] S. Lin, H. Yuan, X. Huang, A computational study on the quenching and near-limit propagation of smoldering combustion, Combust. Flame 238 (2022) 111937.

[35] N.A. Lutsenko, Numerical model of two-dimensional heterogeneous combustion in porous media under natural convection or forced filtration, Combust. Theor. Model. 22 (2018) 359–377.

[36] V. Pozzobon, G. Baud, S. Salvador, G. Debenest, Darcy scale modeling of smoldering: impact of heat loss, Combust. Sci. Technol. 189 (2017) 340–365.

[37] M. Moallemi, H. Zhang, S. Kumar, Numerical modeling of two-dimensional smoldering processes, Combust. Flame 95 (1993) 170–182.

[38] C. Ghabi, H. Benticha, M. Sassi, Computational modelling and simulation of forward-smouldering of porous media in a fixed bed, Progr. Comput. Fluid Dyn. Int. J. 7 (2007) 283–293.

[39] J. Yang, N. Liu, H. Chen, W. Gao, R. Tu, Effects of atmospheric oxygen on horizontal peat smoldering fires: experimental and numerical study, Proc. Combust. Inst. 37 (2019) 4063–4071.

[40] R. Solinger, G.P. Grant, G.C. Scholes, C. Murray, J.I. Gerhard, STARx Hottpad for smoldering treatment of waste oil sludge: proof of concept and sensitivity to key design parameters, Waste Manage. Res. 38 (2020) 554–566.

[41] J. Wang, M.A. Zanoni, J.L. Torero, J.I. Gerhard, Understanding the role of water evaporation and condensation in applied smoldering systems, Combust. Flame 253 (2023) 112780.

[42] C. Switzer, P. Pironi, J.I. Gerhard, G. Rein, J.L. Torero, Self-sustaining smoldering combustion: a novel remediation process for non-aqueous-phase liquids in porous media, Environ. Sci. Technol. 43 (2009) 5871–5877.

[43] S. Arrhenius, Über die Reaktionsgeschwindigkeit bei der Inversion von Rohrzucker durch Säuren, Wilhelm Engelmann (1889).

[44] B.H. Kueper, E.O. Frind, Two-phase flow in heterogeneous porous media: 1. Model development, Water Resour. Res. 27 (1991) 1049–1057.

[45] J. Gerhard, B. Kueper, Capillary pressure characteristics necessary for simulating DNAPL infiltration, redistribution, and immobilization in saturated porous media, Water Resour. Res. 39 (2003).

[46] J. Gerhard, B. Kueper, Relative permeability characteristics necessary for simulating DNAPL infiltration, redistribution, and immobilization in saturated porous media, Water Resour. Res. 39 (2003).

[47] É. Clapeyron, Mémoire sur la puissance motrice de la chaleur, Jacques Gabay (1834).

[48] M.A.B. Zanoni, J. Wang, J.I. Gerhard, Understanding pressure changes in smouldering thermal porous media reactors, Chem. Eng. J. 412 (2021) 128642.

[49] T.L. Rashwan, J.L. Torero, J.I. Gerhard, Heat losses in applied smouldering systems: sensitivity analysis via analytical modelling, Int. J. Heat Mass Transfer 172 (2021) 121150.

[50] M.A. Zanoni, J.L. Torero, J.I. Gerhard, The role of local thermal non-equilibrium in modelling smouldering combustion of organic liquids, Proc. Combust. Inst. 37 (2019) 3109–3117.

[51] M.A. Zanoni, J.L. Torero, J.I. Gerhard, Determination of the interfacial heat transfer coefficient between forced air and sand at Reynold's numbers relevant to smouldering combustion, Int. J. Heat Mass Transfer 114 (2017) 90–104.

[52] S. Rosseland, Astrophysik: Auf atomtheoretischer Grundlage, Springer-Verlag, 2013.

[53] F.P. Incropera, A.S. Lavine, T.L. Bergman, D.P. DeWitt, Fundamentals of Heat and Mass Transfer, Wiley 2007.

[54] E.E.G. Rojas, J.S. Coimbra, J. Telis-Romero, Thermophysical properties of cotton, canola, sunflower and soybean oils as a function of temperature, Int. J. Food Properties 16 (2013) 1620–1629.

[55] J.L. Torero, A.C. Fernandez-Pello, M. Kitano, Opposed forced flow smoldering of polyurethane foam, Combust. Sci. Technol. 91 (1993) 95–117.

[56] D. PERRY, Chemical Engineers Handbook, McGraw-Hill, Kansas/EUA, 1999.

[57] M.A.B. Zanoni, J.L. Torero, J.I. Gerhard, Determination of the interfacial heat transfer coefficient between forced air and sand at Reynold's numbers relevant to smouldering combustion, Int. J. Heat Mass Transf. 114 (2017) 90–104.

[58] L. Yermán, H. Wall, J.L. Torero, Experimental investigation on the destruction rates of organic waste with high moisture content by means of self-sustained smouldering combustion, Proc. Combust. Inst. 36 (2017) 4419–4426.

[59] L. Yermán, H. Wall, J. Torero, J. Gerhard, Y.-L. Cheng, Smoldering combustion as a treatment technology for feces: sensitivity to key parameters, Combust. Sci. Technol. 188 (2016) 968–981.

[60] P. Pironi, C. Switzer, G. Rein, A. Fuentes, J.I. Gerhard, J.L. Torero, Small-scale forward smouldering experiments for remediation of coal tar in inert media, Proc. Combust. Inst. 32 (2009) 1957–1964.

[61] G. Baud, S. Salvador, G. Debenest, J.-F. Thovert, New granular model medium to investigate smoldering fronts propagation experiments, Energy Fuels 29 (2015) 6780–6792.

[62] M.A. Zanoni, J. Wang, J.I. Gerhard, Understanding pressure changes in smouldering thermal porous media reactors, Chem. Eng. J. 412 (2021) 128642.

[63] D. Gutierrez, F. Skoreyko, R. Moore, S. Mehta, M. Ursenbach, The challenge of predicting field performance of air injection projects based on laboratory and numerical modelling, J. Can. Petroleum Technol. 48 (2009) 23–33.

[64] M.F. Martins, S. Salvador, J.F. Thovert, G. Debenest, Co-current combustion of oil shale - Part 2: structure of the combustion front, Fuel 89 (2010) 133–143.

[65] T.L. Rashwan, T. Fournie, M. Green, A.L. Duchesne, J.K. Brown, G.P. Grant, J. L. Torero, J.I. Gerhard, Applied smouldering for co-waste management: benefits and trade-offs, Fuel Process. Technol. 240 (2023) 107542.

[66] G.S. Kumar, D.S. Reddy, Numerical modelling of forward in-situ combustion process in heavy oil reservoirs, Int. J. Oil Gas Coal Technol. 16 (2017) 43–58.

[67] L.L. Kinsman, Smouldering Remediation: Transient Effects of Front Propagation, The University of Western Ontario, Canada, 2015.